Annual Adjustment of the Thermocline in the Tropical Pacific Ocean

BIN WANG, RENGUANG WU, AND ROGER LUKAS

Department of Meteorology and International Pacific Research Center, School of Ocean and Earth Science and Technology, University of Hawaii, Honolulu, Hawaii*

(Manuscript received 8 September 1998, in final form 13 April 1999)

ABSTRACT

In this paper the amplitude-phase characteristics of the annual adjustment of the thermocline in the entire tropical Pacific Ocean are described and numerical experiments with a tropical ocean model are performed to assess the roles of the major wind systems in controlling the annual variation of the thermocline.

In the region between about 8°N and 10°S, the annual adjustment of the thermocline is controlled by both the Ekman pumping and equatorial wave propagation. The local wind stress forcing plays a dominant role in the central North Pacific (3°–8°N, 170°–120°W) where the thermocline exhibits the largest amplitude due to the prominent annual variation of the wind stress curl south of the ITCZ. In the equatorial central Pacific (2°N–5°S, 170°–120°W), the annual cycle also exhibits a pronounced unimodal seasonal variation (deepest in December and shallowest in May–June). This distinctive annual cycle results primarily from the adjustment of the waves, which are excited around 4°N, 110°W by the annual march of the ITCZ and excited in the equatorial western Pacific by the monsoon flows. The December maximum and May–June minimum then propagate westward in the off-equatorial waveguides along 5°N (3°–7°N) and 6°S (3°–9°S) to the western boundary. These annual Rossby waves are reflected at the western ocean boundary. The bimodal annual variation in the equatorial western Pacific is caused by the combined effects of the annual Rossby wave reflection and the monsoon westerly forcing during transitional seasons. The bimodal variations in the equatorial far eastern Pacific are determined by the remote forcing through the eastward propagation of Kelvin waves.

The thermocline variations in the North Pacific poleward of 8°N and in the South Pacific poleward of 10°S form approximately an annual seesaw oscillation with maximum depth occurring in May–June (October–November) and minimum in December (April–May) in the North (South) Pacific. These regions are characterized by an Ekman regime.

1. Introduction

Thermocline depth variations play a key role in El Niño–Southern Oscillation (ENSO). They ''memorize'' the changes in the surface winds and provide a delayed feedback, which may be critical in turning the coupled ocean–atmosphere system around from warm to cold state or vice versa (Zebiak and Cane 1987). On the annual and interannual timescales, the Pacific thermocline variations exhibit distinctive features and different impacts on sea surface temperature (SST) due to the different physical processes involved (Chang 1994). The relationship between the annual and interannual variations of the thermocline is not well known. Understanding the causes of the annual variation of the depth of thermocline (DTC) is thus necessary to better understand short-term climate variation in the tropical Pacific.

Meyers (1979a,b) studied the annual variation of the thermocline represented by the 14°C isotherm depth determined from expendable bathythermograph (XBT) data. He found annual Rossby waves propagating westward along 6°N in the central and western Pacific. Kessler (1990) updated Meyers' work by adding more than 10 yr of mechanical bathythermograph data in the western North Pacific. He found that the DTC (defined by the depth of the 20°C isotherm) propagates westward across the basin as a long Rossby wave near 5°N and 14°–18°N, while the annual cycle around 10°N is dominated by local Ekman pumping. The westward propagation of annual Rossby waves in the western Pacific were confirmed by sea level observations along 7°N (Mitchum and Lukas 1990), by Tropical Atmosphere–Ocean (TAO) buoy observations at 5°N and 5°S (Kessler and McPhaden 1995; Yu and McPhaden 1999) and by TOPEX/Poseidon satellite altimeter observations along 4°N (Chelton and Schlax 1996; Boulanger and Fu 1996). In the equatorial waveguide, the thermocline variation in the eastern Pacific was significantly influenced by

* IPRC is sponsored in part by Frontier Research System for Global Change.

Corresponding author address: Dr. Bin Wang, Department of Meteorology, School of Ocean & Earth Science & Technology, University of Hawaii, 2525 Correa Road, Honolulu, HI 96882-2219.
E-mail: bwang@soest.hawaii.edu

annual Kelvin waves (Lukas 1981) and remotely forced westward and upward (phase) propagating annual Rossby waves (Lukas and Firing 1985; Kessler and McCreary 1993). The thermocline variations along the equator showed primarily eastward propagation (e.g., Yu and McPhaden 1999), but some hint of westward propagation was also reported (Yang et al. 1997).

The severe undersampling of subsurface variability has been a major obstacle in describing Pacific *basinwide* adjustment of the thermocline. There is virtually no reliable information about the annual variation of the thermocline in the South Pacific, because the XBT data are distributed primarily along a few ship lines, and large gaps exist in the South Pacific (cf. Kessler 1990). Due to the limited quantity and quality of subsurface data, the previous analyses of annual wave propagation are primarily made along selected latitudes. The wave rays do not follow constant latitudes due to the beta-dispersion. The reflection of the waves at the boundaries cannot be detected by examining signals at constant latitudes. To better understand the roles of the local wind forcing versus propagation of remotely forced waves in thermocline adjustment, we need to describe the two-dimensional *phase propagation* of the *annual* thermocline displacement and to delineate transition regions between different regimes of the annual thermocline adjustment.

The first purpose of the present study, therefore, is to address the gaps in our observational description of the annual thermocline variations. The National Centers for Environmental Prediction (NCEP) Ocean Data Assimilation System (ODAS; Ji et al. 1995) provides a much improved dataset for examination of Pacific *basinwide* thermocline variability. We will use this dataset to document the *amplitude and phase characteristics* of the annual variation of the thermocline in the entire tropical Pacific Ocean between 20°N and 20°S. The analysis technique adopted has been effectively used in the analysis of annual cycles of meteorological fields. The analysis will detect regions of sharp changes in the characteristics of the annual variation and use these discontinuities to define transitional zones between different regimes of annual variation. Such a coherent phase map provides us with much more new information than those showed by individual longitude–time diagrams.

Previous studies have shown that the dynamics of the annual thermocline adjustment are governed by the local response to wind forcing via Ekman pumping and by the propagation of the Rossby and Kelvin waves, which are generated by remote wind forcing (Meyers 1979a,b; Kindle 1979; Busalacchi and O'Brien 1980; Kessler 1990; Kessler and McCreary 1993; Minobe 1996; Yang et al. 1997; Yu and McPhaden 1999). However, the relative importance of the two mechanisms is not certain in some regions of the Pacific. In the equatorial region, Yu and McPhaden (1999) concluded that the sum of the Rossby waves and the first two baroclinic Kelvin waves results in annual eastward propagation of DTC, whereas Yang et al. (1997) suggested that the eastward propagation of the DTC variation is mainly related to the abrupt changes during the annual relaxation/intensification period of the easterly wind stress. The equatorial Pacific is a region that is directly affected by the monsoon in the western Pacific and the trade winds associated with the intertropical convergence zone (ITCZ). Both wind systems have prominent annual variations. The equatorial Pacific is also a region where equatorial Kelvin and Rossby waves can adjust the thermocline efficiently due to the relatively fast wave propagation speed. It is not clear how these waves are forced by the annual march of the ITCZ and western Pacific monsoons. In general, what remains unclear is how the wind variability in the key regions of the Pacific determines the thermocline variations in the equatorial Pacific and other regions of the tropical Pacific basin. The second purpose of this study is to address these concerns through numerical experiments with a model that can realistically simulate the annual variation of thermocline.

In the following section, we will first discuss an important issue regarding the definition of DTC using subsurface temperature data. A comprehensive amplitude-phase characteristic analysis of the observed annual thermocline variation is presented in section 3. The results delineate the boundaries between the local forcing-dominant and wave adjustment–dominant regimes in terms of the minimum of the annual harmonics and maximum bimodal variations. Sections 4–6 interpret observations. We first examine the relationship between local wind forcing and thermocline variation in section 4, then conduct numerical experiments with an intermediate tropical ocean model to assess the sensitivity of the thermocline adjustment to the forcing provided by major wind systems in section 5, and finally discuss the factors governing the annual variation of thermocline depth in the equatorial Pacific between 8°N and 10°S in section 6. The last section summarizes our results and discusses implications of the results for short-term climate variability.

2. Data and the definition of the thermocline depth

a. Data

The ocean temperature and surface wind stress data that are used in the present study span from January 1980 to December 1995. They were obtained from the dataset (version RA6) assimilated at the NCEP (Leetmaa and Ji 1989; Ji et al. 1995). The ODAS uses all available thermal observations throughout the basin, including SST measured from ships, buoys, and satellites (Reynolds and Smith 1994) and subsurface temperature measured from XBTs and moored buoys. The ocean model used is an ocean general circulation model originally developed at the Geophysical Fluid Dynamics Labo-

ratory (Bryan 1969; Cox 1984; Philander et al. 1987). The observed temperature data are assimilated into the model using the method described by Derber and Rosati (1989). Currents are obtained from the ocean model driven by observed wind stress and surface heat fluxes and constrained by observed temperature observations. The climatological annual cycle of wind stress was constructed from Harrison (1989) between 20°S and 20°N and Hellerman and Rosenstein (1983) poleward of 30° lat, with a linear interpolation between 20° and 30° lat. The anomalous wind stress was derived from The Florida State University analysis (Goldenberg and O'Brien 1981). The surface heat flux forcing is the climatology of Oberhuber (1988) but the assimilated SST controls the ODAS SST. In the data void regions, the ocean model provides interpolations consistent with the model physics. The reliability of the products depends on the density of the observations assimilated into the model and the model physics. Evaluations of the ODAS products can be found in Ji et al. (1995). The data assimilated into the model change with time, especially due to the growth of the TAO buoys. Thus, the ODAS product is more reliable after 1992.

Smith and Chelliah (1995) described the mean annual cycle of subsurface temperature variability by using harmonic analysis. Their comparison with observations showed that the reanalysis captures *large-scale* ocean thermal variations reasonably well. Ji et al. (1995) analyzed the main spatial modes of both annual and interannual sea level variability. The annual modes reveal the signals of equatorially trapped Rossby waves.

Climatological monthly mean time series are first computed for each of the 1° lat × 3° long grid. To describe large-scale features, smoothed 2° lat × 9 ° long grid data are also produced by simple area average.

b. Definition of the thermocline depth

From the ocean dynamic point of view, the vertical displacement of the thermocline in response to varying wind stress forcing is of great importance. An issue arises concerning how to objectively define the DTC and estimate it observationally. Both the upper-ocean heat content and the sea surface height have been used as a proxy to estimate thermocline variations. These quantities reflect vertical integrated property of upper ocean (and the deep ocean in the case of sea level) thermal fields including mixed-layer thermodynamics and are not direct measures of the thermocline displacement, which results primarily from upper-ocean dynamics. Given the strength of the reanalysis dataset, that is, the subsurface temperature assimilation, it is desirable to define the DTC directly based on the vertical distribution of thermal field.

The thermocline layer is characterized by a large vertical temperature gradient. Thus, it would be natural to take the depth of the maximum vertical temperature gradient as the DTC. This, however, is practically difficult because vertical resolution of observations and models are often not sufficient to resolve the maximum gradient. An additional problem we have encountered is that, in the warm pool and trade wind regions, the maximum vertical gradients are sometimes located at the upper portion of the thermocline layer (close to the bottom of the mixed layer) and thus do not represent the center of the thermocline layer. Probably for the same reasons, the DTC was represented in the past simply by the depth of a ''representative'' isotherm (20°C or 14°C) within the thermocline layer. While the 20°C isotherm is suitable for the warm pool, it fails for the cold tongue and coastal upwelling regions, because the 20°C isotherms may surface during the cold season. On the other hand, the 14°C isotherm is much too deep to represent the warm pool thermocline temperature. We, therefore, will not follow these conventional definitions using an isotherm of a fixed temperature.

The observed representative temperature at the central depth of the thermocline varies with location. We, therefore, propose to use a location-dependent representative temperature T_c to characterize the temperature at the center of the thermocline layer. The temperature at 350 m shows small horizontal variation between 20°N and 20°S (except the gradients associated with the two subtropical gyres in the western-central Pacific poleward of 10° lat) with an average temperature of about 12°C (Fig. 1a). It is, therefore, reasonable to define a representative thermocline temperature by averaging 12°C (representing the temperature at the base of the thermocline layer) and the local long-term mean SST (representing the temperature at the top of the thermocline). Such defined representative temperature T_c varies from 20.5°C in the warmest places to about 16°C near the Peru coast in the tropical region between 20°S and 20°N (Fig. 1b). Examination of a large number of vertical profiles obtained from various regions of the tropical Pacific indicates that the depth of T_c better represents the central depth of the thermocline layer than that of 20°C or 14°C isotherms. The DTC defined here can be thought of as an idealized interface in an equivalent two-layer system. It thus facilitates the comparison of the DTC with the upper-ocean dynamical response to surface wind forcing in a reduced gravity ocean model.

Our correlation study shows that the depth of T_c is highly correlated with the 20°C isotherm depth except off the coast of Peru (Fig. 2a) where the 20°C isotherm is too shallow to adequately represent the mean depth of the thermocline layer. The DTC is also highly correlated with the 14°C isotherm except in the far eastern equatorial Pacific and in the vicinity of New Guinea (Fig. 2b) where the 14°C isotherm is too deep to adequately represent the mean depth of the thermocline. The DTC is very well correlated with the upper-ocean heat storage above 400 m within the Tropics between 15°N and 15°S except in a part of the southeast Pacific (Fig. 2c) where the thermocline layer is ill-defined and

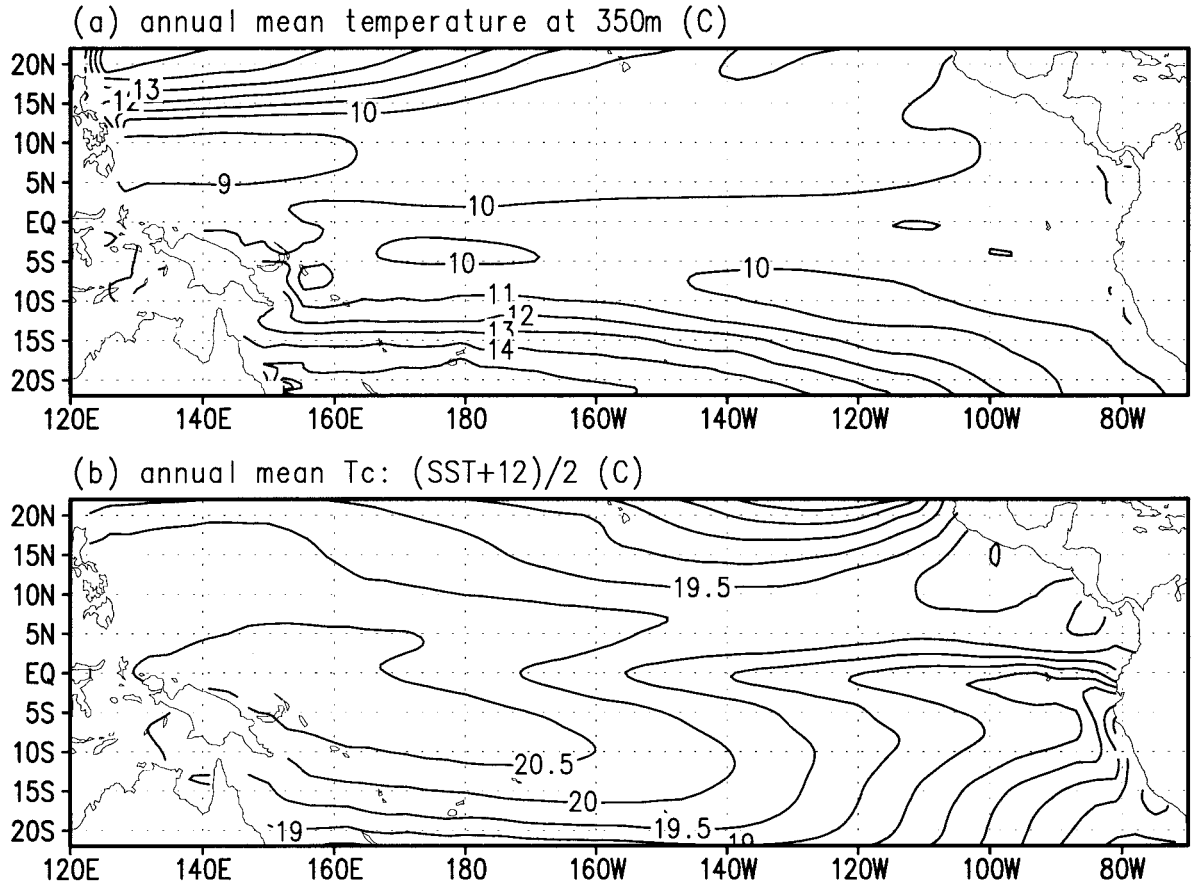

FIG. 1. Distribution of (a) the long-term mean temperature (°C) at 350-m depth, and (b) the representative temperature (°C) at the middle of the thermocline layer defined by average of 12°C and the long-term mean SST.

the seasonal variation of the mixed-layer thermodynamics has large impact on the upper-ocean heat storage.

3. The observed annual basinwide adjustment of the thermocline

In this section we focus on the analysis of the amplitude and phase characteristics of the basinwide adjustment of the thermocline on annual timescales. For completeness and convenience of discussion, we will first briefly describe the features of the climatological mean, annual range, and characteristic seasonal variation (unimodal and bimodal), then describe the basinwide phase distribution and evolution of the annual departure from the mean.

a. The long-term mean and annual range

The long-term mean DTC in the tropical Pacific is shown in Fig. 3a. The mean thermocline is characterized by overall eastward shoaling in response to the prevailing westward wind stress of the trades. The areas of deep thermocline north of 15°N and south of 15°S are not symmetric about the equator: the one in the southern flank of the warm pool is deeper, wider, and closer to the equator in the western Pacific, whereas the one in the northern edge of the warm pool is separated from the equator by the *North Equatorial Counter Current (NECC) ridge* along about 7°–10°N. This ridge separates the North Equatorial Current (NEC) and the NECC and inhibits meridional transfer of water except in the Mindanao Current region. In between the two trade wind thermocline troughs, zonally oriented ridges and troughs also display a prominent *latitudinal asymmetry* with regard to the equator. The *Counter Current Trough* centered between 3° and 5°N divides the NECC and the South Equatorial Current (Wyrtki 1974). A broad *equatorial ridge* in the eastern Pacific is slightly biased to the south of the equator, corresponding to the core of the equatorial cold SST tongue. The shallowest mean thermocline in the western Pacific warm pool is not located at the equator, but around 7°N, because of the upwelling associated with the Mindanao Eddy (Wyrtki 1961; Lukas et al. 1991; Masumoto and Yamagata 1993). The mean depth shown here is in very good agreement with the mean sea level topography compiled by Wyrtki (1975) and agrees well with that derived by Kessler (1990) using 20°C isotherm depth

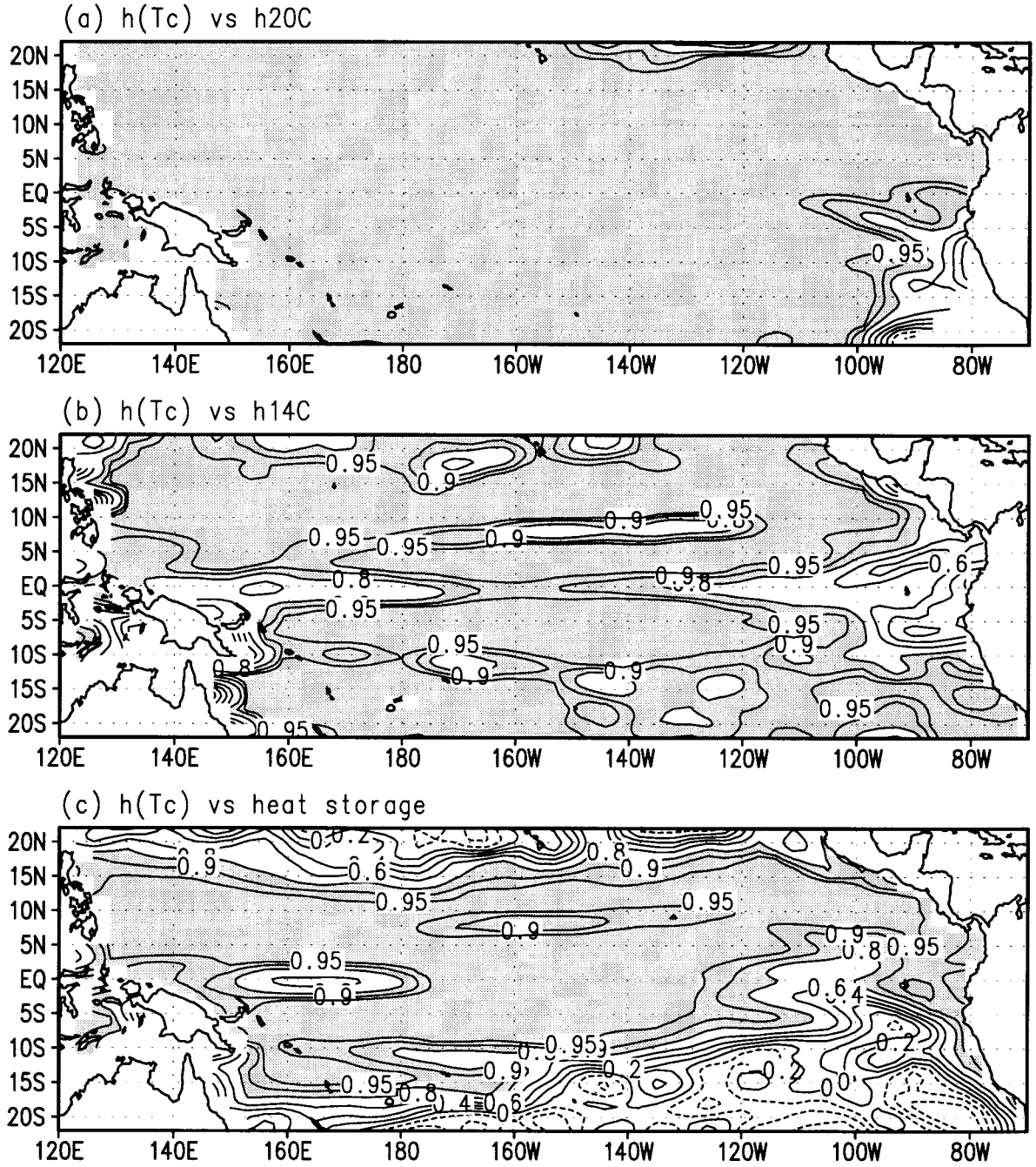

FIG. 2. Correlation maps of the thermocline depth defined in this study with (a) the depth of the 20°C isotherm, (b) the depth of the 14°C isotherm, and (c) the heat storage above 400 m. Contour interval is 0.20 for correlations below 0.8. Contours for correlation of 0.9 and 0.95 are also plotted. The shading indicates regions where the correlation coefficients exceed 0.80.

except in the southeast Pacific where the 20°C is much shallower as discussed in the previous section.

The magnitude of annual variation of the DTC may be measured by the annual range (the difference between the maximum and minimum depth), which is shown in Fig. 3b. The standard deviation of the annual variation of DTC exhibits a very similar spatial distribution (figure not shown). The area of the most prominent annual variability is found in the eastern-central Pacific residing on both sides of the mean position of the ITCZ. In this region, the variability of the annual cycle is comparable with that of the interannual variations (Fig. 3c). The largest annual variability is centered at 4°N, 140°W. Other regions of prominent annual variability are found in the western North Pacific and south of the South Pacific convergence zone (SPCZ) west of the date line. The

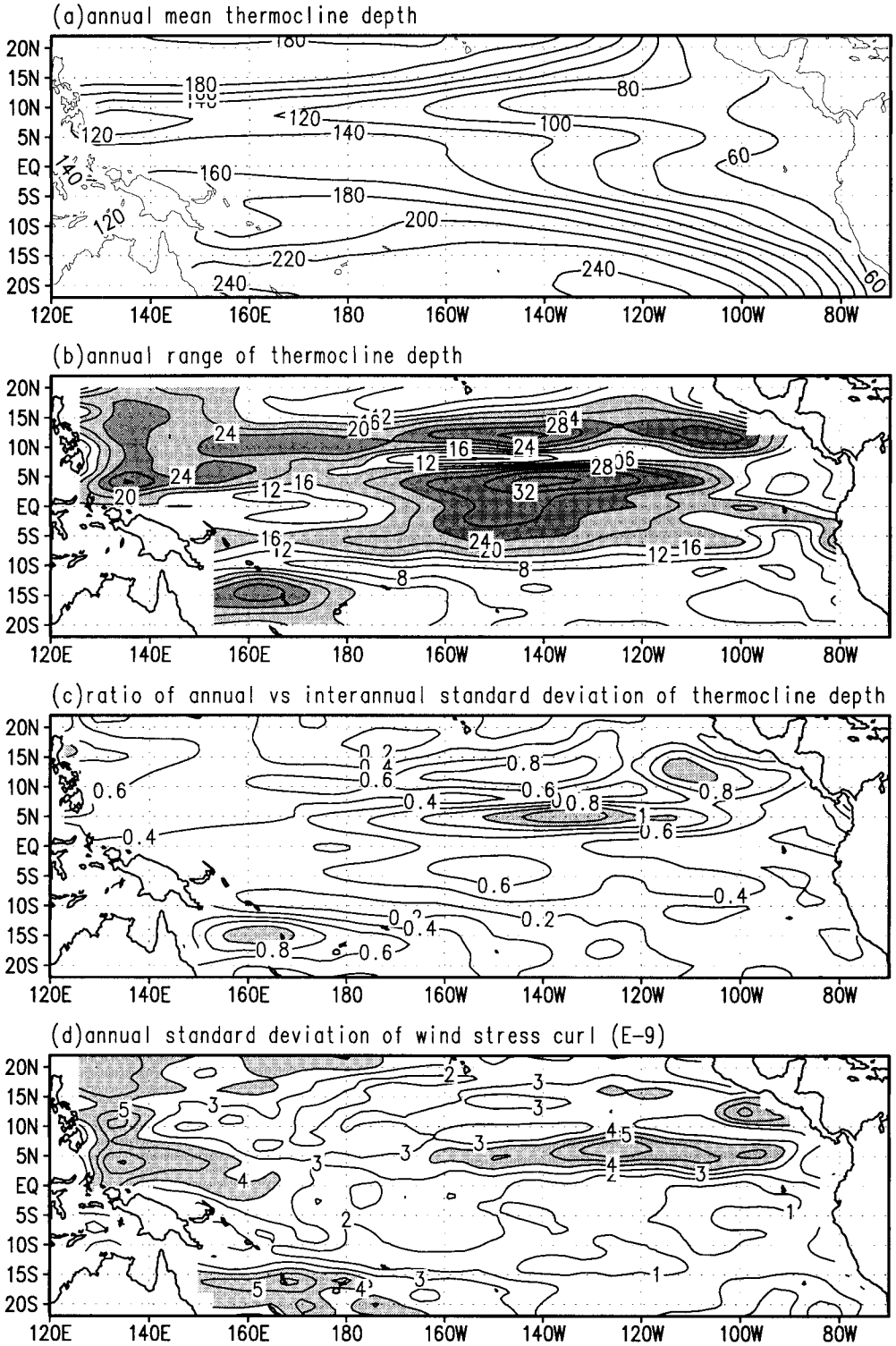

FIG. 3. Observed climatology of the thermocline depth in the tropical Pacific: (a) the mean depth (m); (b) the annual range (maximum − minimum) in units of meter with light and dark shading denoting regions where the annual range is between 16 m and 24 m and exceeds 24 m, respectively; (c) the ratio of the annual vs interannual standard deviation of the thermocline depth; and (d) the annual standard deviation of wind stress curl in units of 10^{-9} Nm^{-3}, where areas of high standard deviation are shaded.

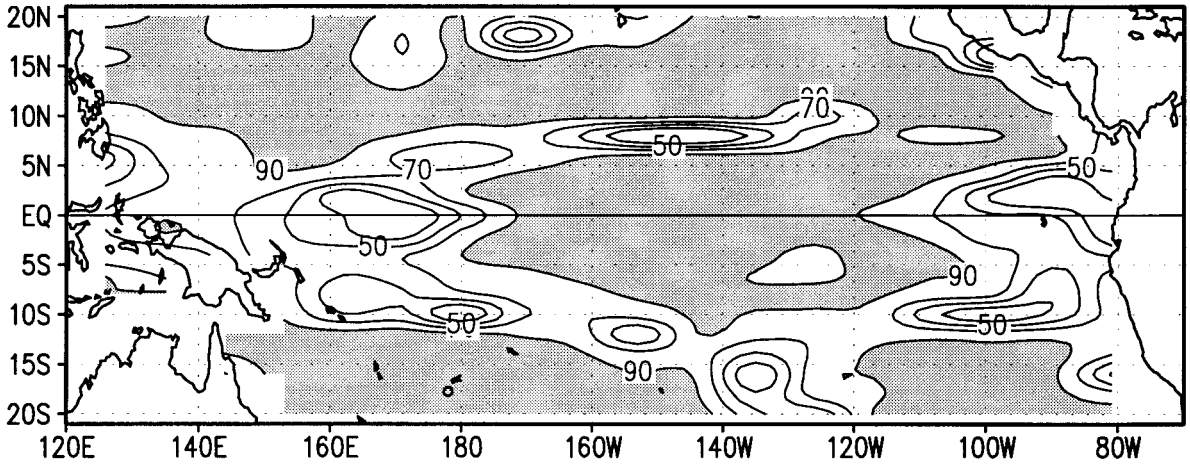

FIG. 4. Percent variance of the annual harmonic on 9° × 2° grids. Regions with the percent variance exceeding 90% are shaded.

equatorial central Pacific between 170°W and 120°W also exhibits large annual variability. This prominent annual variability, however, is missing in Kessler's (1990) analysis. In general, the annual range shown in Fig. 3b differs substantially from Kessler's (1990) results in the equatorial regions between 10°S and 10°N where the early XBT data have large spatial gaps. The data we used here include the recent period during which the observations have rapidly increased due to implementation of the TAO buoys and the prolonged 1991–94 warm event occurred. The discrepancy is primarily attributed to the effects of several strong El Niños in the study period. The other reason is the better data coverage in the equatorial Pacific from TAO array.

The annual range of the thermocline (Fig. 3b) tends to be closely correlated with the annual standard deviation of the surface wind stress curl shown in Fig. 3d except around 10°–15°N, 140°W. In the eastern North Pacific, the two belts of maximum variability are associated with the maximum variability of the wind stress curl on both sides of the mean ITCZ though south of the ITCZ remotely forced equatorial waves also contribute to the thermocline variability. The large thermocline variations over the western North Pacific and south of the mean SPCZ are also associated with prominent variations in the local wind stress curl. These wind variations result, respectively, from the seasonal variations of the western Pacific monsoon and the annual march of the SPCZ. The above results suggest critical roles of the ITCZ and western Pacific monsoon in the annual thermocline displacement outside the equatorial waveguide. As in the long-term mean field, the annual range also exhibits remarkable *latitudinal asymmetry;* larger ranges occur in the North Pacific. This latitudinal asymmetry is essentially caused by the latitudinal asymmetry in the trade winds and their associated ITCZ. The ITCZ is permanently situated in the Northern Hemisphere around 8°N with a most significant annual march around 110°W from 3°N in March to 12°N in August (Murakami et al. 1992).

b. The unimodal and bimodal annual variations

The annual variation of the DTC in the tropical Pacific is primarily characterized by a unimodal variation, that is, the first annual harmonic is the dominant component and there are a single maximum and a single minimum during the course of the year. The percent variance of the first annual harmonic in these regions exceeds 90% of the total annual variance (Fig. 4). In most cases, when the percent variance accounted for by the first annual harmonic is below 50%, the annual cycle features a bimodal variation, that is, there are double maxima and minima during the course of the year.

The bimodal regime results from the influences from two adjacent regions and represent transitional zones in between two different regimes of the annual cycle (Wang 1994). The double maxima (minima) of bimodal variation reflect the merging of two different unimodal regimes that have different timing for their maxima (minima). The zones of bimodal variation have small annual range (Fig. 3b). For instance, the regions where the percent variance of the annual harmonic is less than 70% tend to coincide with the regions of small annual range (less than 16 m). The bimodal variations provide important information for delineating various regimes of annual variations.

Geographically, the zones of bimodal variation are primarily collocated with the mean positions of the ITCZ and SPCZ, and in the *equatorial* western and eastern Pacific (Fig. 4). While the bimodal variation in the eastern Pacific was previously noticed by Meyers (1979b) and Kindle (1979), the significant bimodal variation in the equatorial western Pacific (around 170°E) has not been discussed in the literature. In addition, the bimodal seasonal cycle in sea level near Truk Island

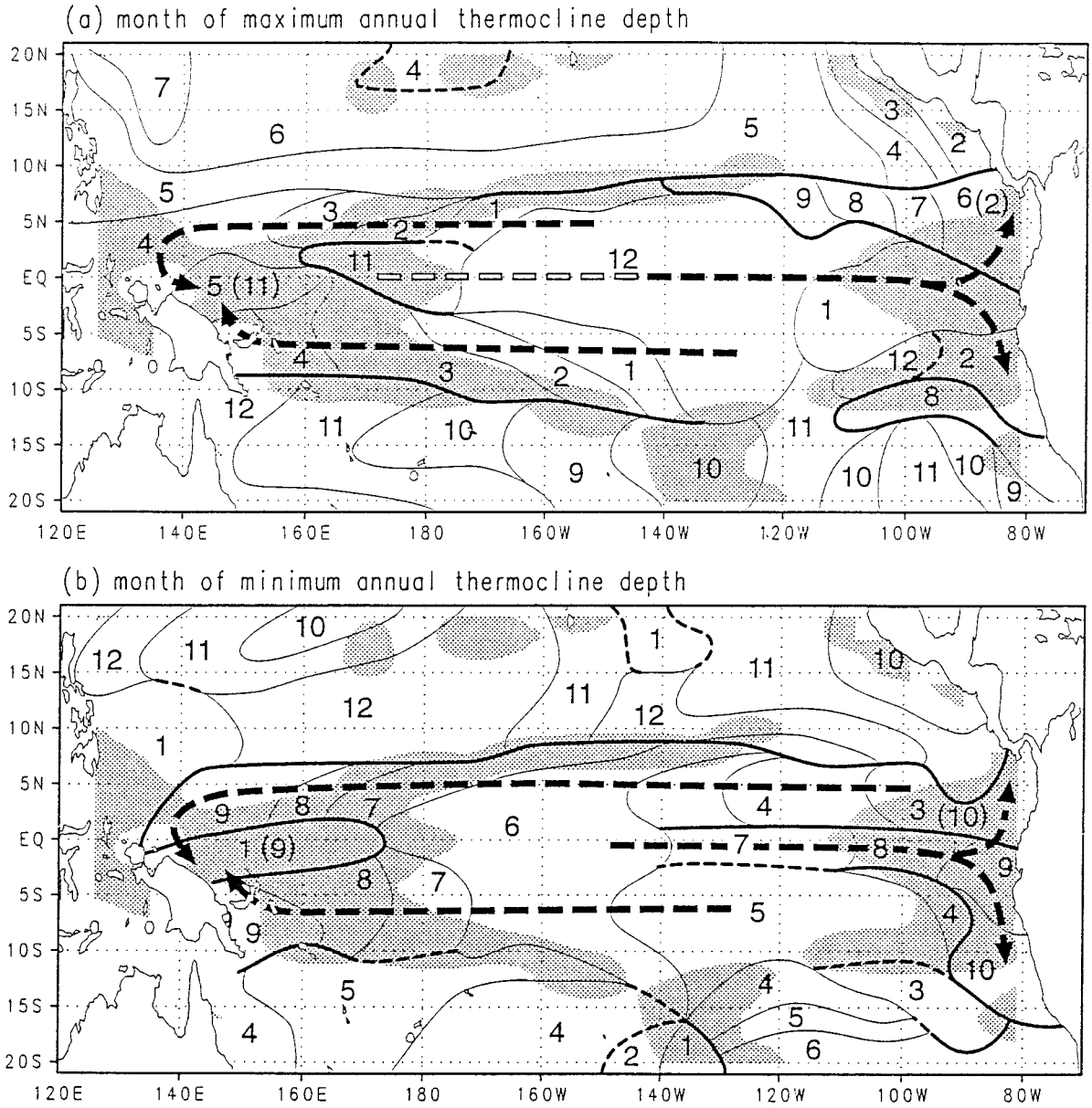

FIG. 5. Phase diagrams showing the month of the calendar year during which the local annual maximum (a) and minimum (b) thermocline depth occurs on 9° × 2° grid. The thick solid lines indicate the phase discontinuity (the phase difference in adjacent grids exceeds 2 months). The thick dashed lines with arrows indicate the routes of phase propagation. Shading indicates regions where the percent variance of the annual harmonic is below 80%. The number in brackets indicate the month during which a secondary maximum (minimum) occurs.

found by Meyers (1982) does not show unambiguously in the present DTC analysis (Fig. 4). The data Meyers used were before 1980, whereas the data we used are after 1980. The annual cycle of sea level near Truk is known to be dominated by ENSO (Mitchum and Lukas 1990). Since the ENSO evolution has experienced a notable change after 1977 (Wang 1995), the difference of the annual variation derived from the two different epochs may reflect the effects of the interdecadal variations.

c. The annual phase propagation

To describe basinwide thermocline adjustment on the annual timescale, we display and discuss the phase diagram. Figures 5a and 5b show the time (calendar months) during which the thermocline reaches the maximum and minimum depth, respectively. They reveal how the local annual variations are related to those at the neighboring regions, providing a picture of the phase propagation of the annual thermocline departure (from

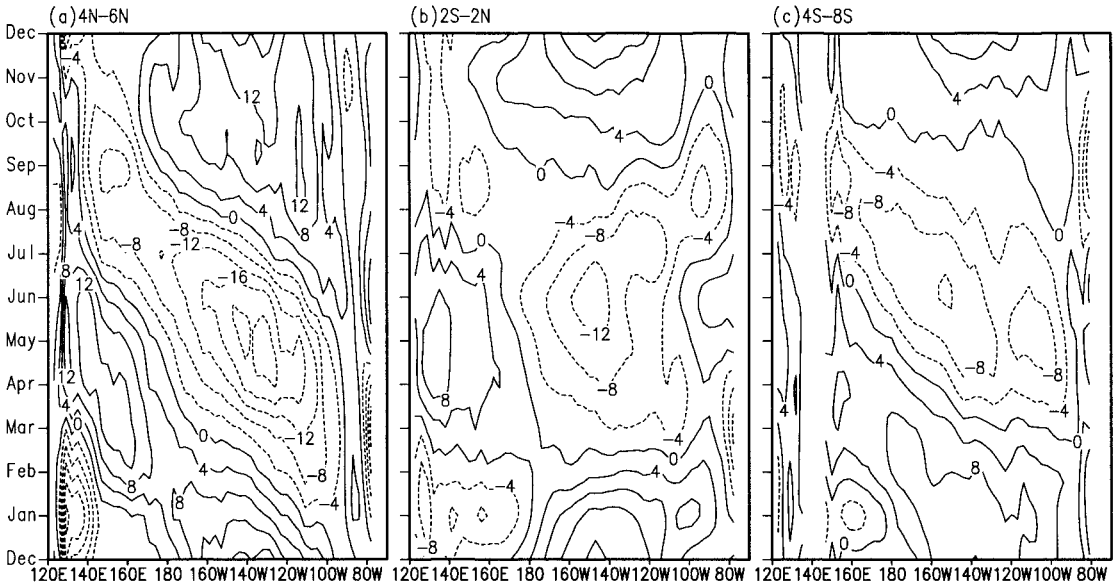

FIG. 6. Time-longitude diagrams of annual thermocline departure (m) along (a) 4°–6°N, the (b) equator (2°S–2°N), and (c) 4°S–8°S.

the annual mean) over the entire tropical Pacific basin. The phase discontinuities (where the phases between two adjacent 9° × 2° grids differ by 3 or more months) occur normally where the annual range is small and the annual variation features bimodal seasonal distribution (Fig. 4). The discontinuities thus mark the narrow transition zones from one regime of annual variation to another.

The off-equatorial trade wind regions in the North and South Pacific poleward of 8°N and 10°S features a nearly in-phase variation, that is, the phases of thermocline variation are latitudinally stationary across the basin except near the American continents. In the North Pacific trade wind regime, the maximum depth occurs in May–June and the minimum depth in November–December (Fig. 5). Due to the paucity of data in the Southern Hemisphere, little has been known concerning the annual variation of the thermocline. Figure 5 reveals that in the South Pacific trade wind regime, the maximum and minimum depths occur in October–November and April–May, respectively. The in-phase variation is similar to the Northern Hemisphere trade wind regime. The phases in the North and South Pacific tend to be 5 months (nearly one-half cycle) out of phase. The annual variation of DTC forms a north–south seesaw between the two hemispheric trade wind regions.

The equatorial regime is most complex and interesting. Its central region covers the vast area of the equatorial central Pacific (ECP; 5°N–5°S, 170°–120°W) where the thermocline is deepest in December and shallowest in May and June (Fig. 5) with pronounced amplitude (Fig. 3b). To the north of the ECP along 5°N, both the annual maximum and minimum depths occur progressively later westward across the basin. The westward phase propagation is particularly systematic for the *annual minimum depth*, which propagates across the entire basin from 100°W to 140°E (Fig. 5b). The annual minimum occurs in March around 100°W and reaches 150°E in September, giving an average phase propagation speed of about 0.80 m s^{-1}. The westward propagation of the annual maximum depth is evident in the western and eastern Pacific but not in the central Pacific (Fig. 5a) where the local wind stress forcing is strong (Fig. 3d). The deepest thermocline occurs in December at 150°W and arrives at 140°E in April with an average phase speed of about 0.75 m s^{-1}. This westward phase propagation is confirmed and clearly identified from the longitude-time diagram averaged along 4°–6°N shown in Fig. 6a. The result here generally agrees with the findings of Meyers (1979a) and Mitchum and Lukas (1990). To the south of the ECP along 6°S, the annual minimum and maximum depths also exhibit westward phase propagation, primarily from 130°W to the coast of New Guinea (150°E), taking about 4 months with an average speed of about 0.80 m s^{-1}. The westward propagation of the DTC departure is confirmed by the Hovmöller diagram along 6°S (4°–8°S) shown in Fig. 6c.

In the equatorial western Pacific around 150°–170°E, the small amplitude annual variation (Fig. 4) displays a bimodal structure: the maximum depth occurs in November and May with minima in January and August–September (Fig. 5). The May maximum (August–September minimum) appears to be a consequence of the westward propagating annual maximum (minimum) depth along 4°–6°N and 4°–8°S, which bends equator-

ward and merges in the equatorial western Pacific in May (August–September). This can be better seen from the evolution of the annual departure shown in the next subsection. This feature has not been previously revealed.

Along the equatorial waveguide between 3°N and 3°S, the annual variation of the DTC shows a mixed standing and eastward propagating pattern (Fig. 5). There is a discernable eastward propagation tendency of the annual maximum depth from 160°E (in November) to 90°W (in January; Fig. 5a). The phase speed is close to that of the lowest baroclinic mode equatorial Kelvin wave. The time of the deepest thermocline in the western Pacific is coincident with the establishment of the strongest Australian monsoon westerlies in November (Sadler et al. 1987). It appears that the thermocline in the equatorial far eastern Pacific is affected by the eastward propagating annual Kelvin waves, which are remotely excited by the western Pacific monsoon (Lukas 1981; Wang 1994). On the Hovmöller diagram (Fig. 6b), the eastward propagation of annual maximum depth is evident mainly in the eastern Pacific from 140°W to the South American coast. The annual minimum depth also propagates eastward during northern summer from 150°W to the coast (Fig. 6b). However, the speed is much slower than that of the maximum depth and cannot be simply attributed to the lowest vertical mode Kelvin wave. The slow propagation speed may be associated with higher vertical mode equatorial Kelvin waves (Yu and McPhaden 1999). Note that the equatorial westward propagation in heat content described by Yang et al. (1997) is not seen from Fig. 5 and barely seen in the western equatorial Pacific in the Hovmöller diagram along the equator (Fig. 6b). The latter may reflect the influence of the westward propagating Rossby waves in the off-equatorial western Pacific.

The southward propagation along the South American coast (Fig. 5) is associated with annual coastal Kelvin waves and their associated reflected Rossby waves. There also exists a northward propagation to the Central American coast, which is not directly evident in Fig. 5, because Fig. 5 depicts only the time of the annual maximum and minimum, while the secondary maximum (minimum) in February (September) of the bimodal variation in the Gulf of Panama is hidden. This bimodal variation actually starts to be evident in the far equatorial eastern Pacific (east of 100°W) (Fig. 6b).

d. Evolution of the thermocline depth departure from the annual mean

To delineate the annual phase propagation revealed by Figs. 5 and 6, we further examine the evolution of the climatological monthly mean departure of DTC from its annual mean.

In December (Fig. 7a), the thermocline reaches maximum depth in the ECP with a departure exceeding 12 m between 160°W and 120°W. The thermocline north of the ITCZ reaches the annual minimum depth. This corresponds to the time of year when the NEC and NECC are strongest (Wyrtki 1974; Philander et al. 1987), because the corresponding meridional slope of the thermocline is largest.

By January (Fig. 7b), the thermocline north of the ITCZ rapidly deepens, while in the far western North Pacific it reaches its annual minimum depths (Fig. 5b). In the ECP, the thermocline starts to rise; meanwhile, the area of positive departure tends to emanate westward as downwelling Rossby waves along about 4°N and 4°S (Fig. 7b). The departures associated with the Rossby waves are responsible for the local annual maximum in January around 5°S in the central Pacific (Fig. 5a). Along the equator, the downwelling Kelvin waves have propagated eastward, arriving at 90°W in January and causing the annual maximum depth in the far eastern equatorial Pacific (Fig. 5a). Over the equatorial western Pacific, however, the thermocline shoals due to the decrease of westerlies, reaching its annual minimum (Fig. 5b). *January is, therefore, the month during which the equatorial thermocline has the smallest east–west slope.* The off-equatorial downwelling Rossby waves continue their westward propagation during February and March, arriving at the western boundary by April (Figs. 7c–e). The thermocline in the northern trade wind regime continues to deepen and becomes deeper than the annual mean by March.

A notable abrupt rise of the thermocline starts at 4°N and 110°W in February and rapidly develops and expands westward in March (Fig. 7d). This happens in the month when the ITCZ reaches its southernmost position and at the longitude where the ITCZ exhibits the largest meridional movement (Murakami et al. 1992). Accompanying the rapid rise is a deepening of the thermocline just to its north and northeast along 12°N. Both the zonally oriented thermocline ridge and trough residing on either side of the ITCZ intensify and expand westward from March to June. Although the rising of thermocline is primarily along 4°N, it expands equatorward and penetrates to the South Pacific from April to June, forming a large negative departure in the ECP by May (Fig. 7f). The rise of the thermocline peaks in June (Fig. 7g). The area of negative departure contains a considerable component that is symmetric about the equator, as is mirrored by the December pattern with opposite signs. The cause of development and subsequent westward and equatorward movement is probably associated with the change of wind stress over the ITCZ and the central Pacific regions. Minobe (1996) detected an annual westward propagation in the eddy (departure from zonal mean) meridional wind component in association with eddy SST gradient between the equator and 10°N, suggesting a coupled nature of the westward and equatorward propagation of the annual maximum (minimum) DTC. This was also suggested by Mitchum and Lukas (1990).

The evolution of the thermocline from July to De-

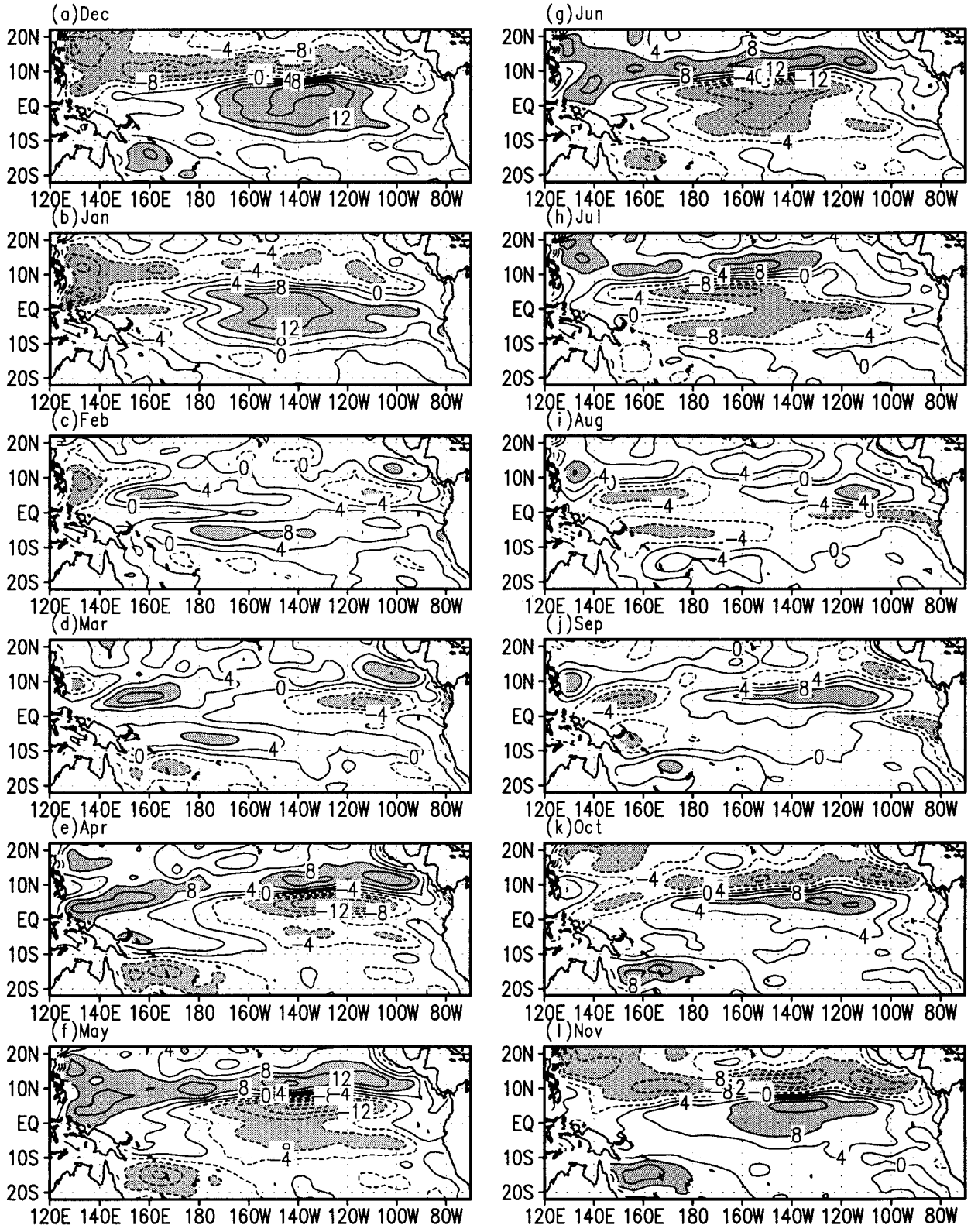

FIG. 7. Climatological monthly mean departures of thermocline depth (m).

cember is almost a mirror image of that from January to June (Figs. 7h–l). The only major difference is found along the equator. The magnitude of the deepening from November to December is stronger than the shoaling in May and June. This is attributed to the western Pacific westerly monsoon maximum occurring in November and its associated eastward propagating downwelling Kelvin waves.

4. Local relationship between Ekman pumping and thermocline displacement

If the local wind stress plays a dominant role in driving thermocline displacement, an upward (a downward) Ekman pumping should lead the thermocline rising (deepening) by about 2–3 months (slightly less than a quadrature of the annual period if the linear damping effect is considered). Figure 8a displays the phase lead of the maximum downwelling Ekman pumping to maximum DTC. Poleward of the mean positions of the ITCZ and SPCZ, the maximum Ekman downwelling generally leads maximum depth of the thermocline by about 1–3 months, indicating a possible controlling role of the local wind stress forcing. Similarly, the maximum upwelling Ekman pumping tends to lead minimum DTC by 1–4 months poleward of the mean ITCZ except the region from 135°W to dateline along 15°N and by 1–3 months in the SPCZ and its poleward side (Fig. 8b).

In the equatorial regime, the wind-induced Ekman pumping generally lags the thermocline variation, especially in the equatorial waveguide, the cold tongue, and the western North Pacific warm pool (west of the dateline and between 8°N and the equator), indicating that the local wind forcing does not play a dominant role in the annual variation of the thermocline. Conversely, equatorial waves must be essential in the annual adjustment of thermocline in this region. Exceptions are found in the central North Pacific (3°–8°N, 170°–110°W) where the Ekman pumping systematically leads the thermocline variation by 1–3 months. This region also displays the largest annual variation of DTC (Fig. 3b) and a distinct unimodal variation (Fig. 4) with a maximum in December and a minimum in May–June (Fig. 5). In this particular area, the annual thermocline variation is likely influenced by the pronounced annual variation in the wind stress curl associated with ITCZ (Fig. 3d).

When the downwelling (upwelling) Ekman pumping lags the thermocline deepening (shoalling), Ekman pumping is not dominant. However, when the Ekman pumping leads the thermocline variation, one cannot rule out the contribution from the wave propagation. The relative importance of different processes cannot be quantitatively determined by examining this phase relationship.

5. Effects of the seasonal migration of the ITCZ and the western Pacific monsoons

a. The ocean model and experiment design

To investigate the role of different wind systems in driving the annual thermocline variation, we employ the intermediate tropical ocean model developed by Wang et al. (1995). The model is nonlinear and consists of two active upper-ocean layers overlaying a deep inert layer: a mixed layer and a baroclinic thermocline layer, both with a variable thickness. The Niiler–Kraus (Niiler and Kraus 1977) mixed-layer parameterization and a simple parameterization for entrained water temperature were used. The model's standard horizontal resolution is 1° lat × 2° long. Higher resolution experiments were also performed to check the sensitivity of results to changes in horizontal resolution. Details of the model formulation and performance are contained in Wang et al. (1995).

A control experiment was first carried out. The model was forced by observed climatological monthly mean wind stress, which consists of an annual mean and a corresponding seasonal departure. The mean wind stress is computed from the mean winds compiled by Sadler et al. (1987) using a constant drag coefficient of 1.3×10^{-3} and air density $\rho_0 = 1.2$ kg m^{-3}. The departure wind stress is derived from NCEP reanalysis. For a better representation of the meridional structure of the thermocline, the diffusion coefficient in the meridional direction is reduced to one-sixth of that in the zonal direction (which is 2.0×10^8 cm^2 s^{-1}) to get a better simulation of the mean thermocline gradient. At the north and south boundaries (30°N and 30°S), the DTC is relaxed back to observed climatological monthly mean. Sensitivity experiments indicate that the annual variation of the thermocline depth between 20°N and 20°S is not sensitive to the specification of the lateral boundary conditions at 30°N and 30°S. The model was run 10 yr and a steady annual cycle was approximately reached.

The simulated mean DTC and annual range in the control experiment (Figs. 9a and 9b) resemble observed counterparts (Figs. 3a and 3b). The largest annual variability is located along 4°N and 12°N in the eastern North Pacific. Large variances extend from south of the mean ITCZ between 160°–120°W equatorward to the ECP. The pronounced westward phase propagation and westward extension of the large variability along 5°N and 6°S are well captured by the model (Figs. 10a and 10c). The eastward propagation of the minimum DTC along the equator is barely discernable (Fig. 10b) but it is evident in the observations (Fig. 6b). The simulated phases along the equator tend to be 1 month ahead of the observed counterpart. Because the mean DTC simulated in the model is deeper than observed, waves propagate faster. In spite of the deficiencies, the overall model simulation is quite realistic, suggesting that the model

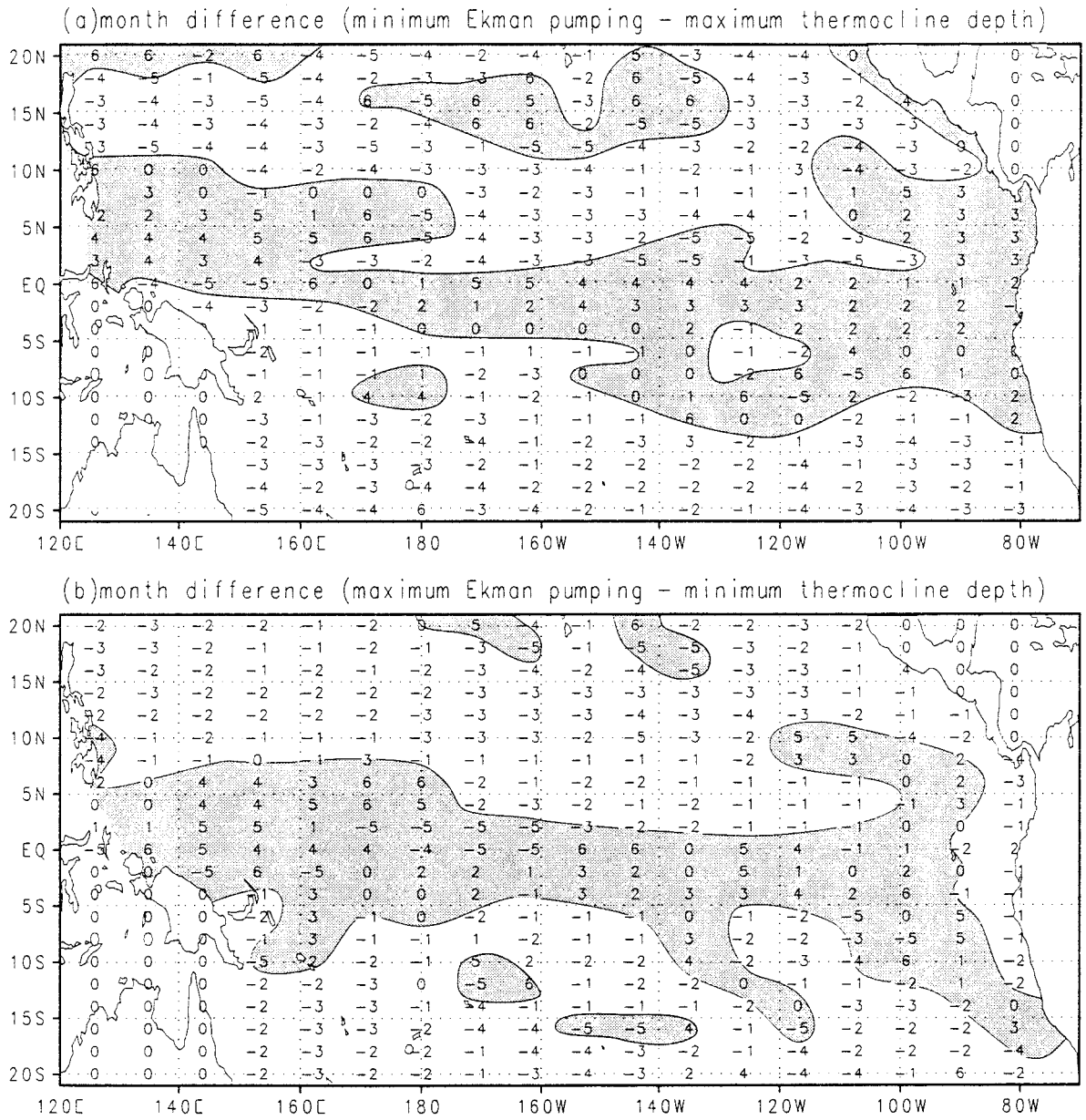

FIG. 8. The phase difference (in units of month) between the minimum Ekman pumping and maximum thermocline depth (a), and between the maximum Ekman pumping and minimum thermocline depth (b). The areas where the minimum (maximum) Ekman pumping leads the maximum (minimum) thermocline depth by 1–4 months are NOT shaded.

contains some of the essential processes governing the annual variation of thermocline.

The largest annual variation of the wind stress in the tropical Pacific shown in Fig. 3d is associated with the annual march of the ITCZ and the monsoons in the western Pacific. East of the dateline, the ITCZ, as outlined by the vanishing meridional wind, migrates from its southernmost position in March around 3°N to its northernmost position in September (Fig. 11). West of the dateline, the westerly summer monsoon shifts from the Southern Hemisphere in December–March to the Northern Hemisphere in June–October with equatorial westerlies prevailing in November and May (Fig. 11). To focus on these two major wind systems, we selected two key regions being named ''ITCZ'' and ''WPM'' (western Pacific monsoon), respectively. Because the response of thermocline depth to the variation of the equatorial wind stress is extremely sensitive, an additional region in the ECP (3°N–3°S, 180°–140°W) is also of interest (Fig. 11).

To reveal the roles of the wind stresses in the above specified regions in driving the annual variation of ther-

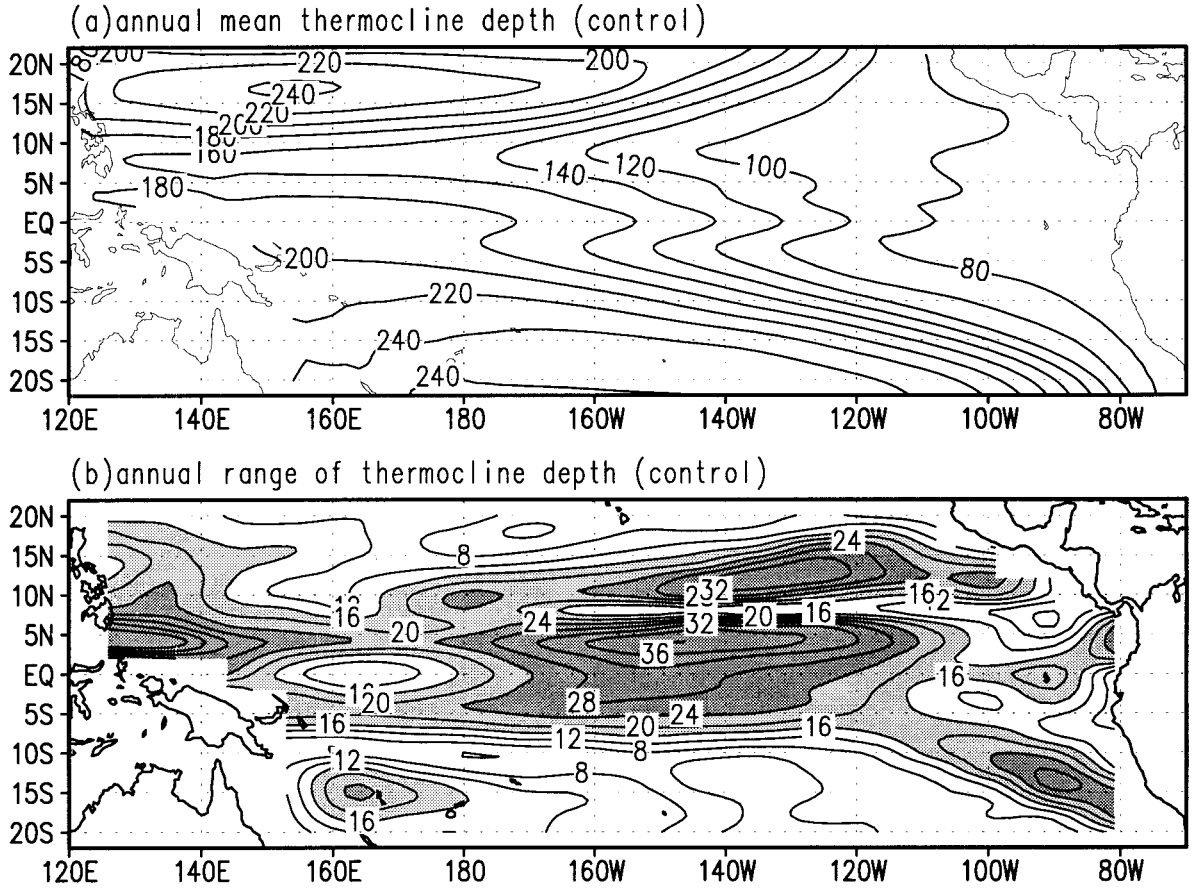

FIG. 9. Annual mean (a) and annual range of thermocline depth (m) on 9° × 2° grid in the control experiment with the intermediate ocean model (Wang et al. 1995) and the Sadler et al. (1987) annual mean wind stress and NCEP's annual departure wind stress forcing.

mocline, we designed two types of experiments that provide complementary information. In the first type, the annual variation of the wind stress is removed in the regions of interest while it is kept elsewhere in the domain. Conversely, in the second type, we keep the annual variation of the wind stress in the regions of interest but completely suppress it elsewhere. For instance, in the ''noITCZ'' experiment (Table 1), the wind stress is replaced by annual mean stress in the key region of the ITCZ. In the ''onlyITCZ'' experiment, the annual variation of the wind stress in the ITCZ region is retained but the wind stress elsewhere is replaced by the annual mean wind stress. To reduce the effect of the discontinuity at the boundary of specified regions, three-point (3° lat) and ten-point (10° long) smoothing was used along the latitudinal and longitudinal boundaries of the region of interest, respectively.

b. Effects of the annual march of ITCZ and western Pacific monsoons

The annual thermocline variation in the eastern North Pacific is determined by local wind stress forcing caused by the annual march of the ITCZ. Without the annual variation of the wind stress associated with the ITCZ, the local thermocline variation is almost totally suppressed (Fig. 12a). The extreme phases also differ fundamentally from those obtained in the control experiment (figure not shown). This is consistent with the inference deduced from the Ekman pumping analysis and confirms the previous observational and simple model studies (Meyers 1979a).

Remotely, the annual march of ITCZ in the eastern Pacific enhances the annual variability in the equatorial western Pacific through excitation of equatorial Rossby waves and reduces the amplitude of the annual variation in the equatorial far eastern Pacific through excitation of Kelvin waves. Whether the annual march of the ITCZ results in an enhancement or a reduction of the annual range in the remote regions depends on the phase relation between the remotely forced waves and the dominant local variations.

The WPM forcing exhibits both local and remote impacts. Locally, the suppression of the WPM (experiment ''noWPM'') leads to a drastic reduction of annual variations over the Philippine Sea and Coral

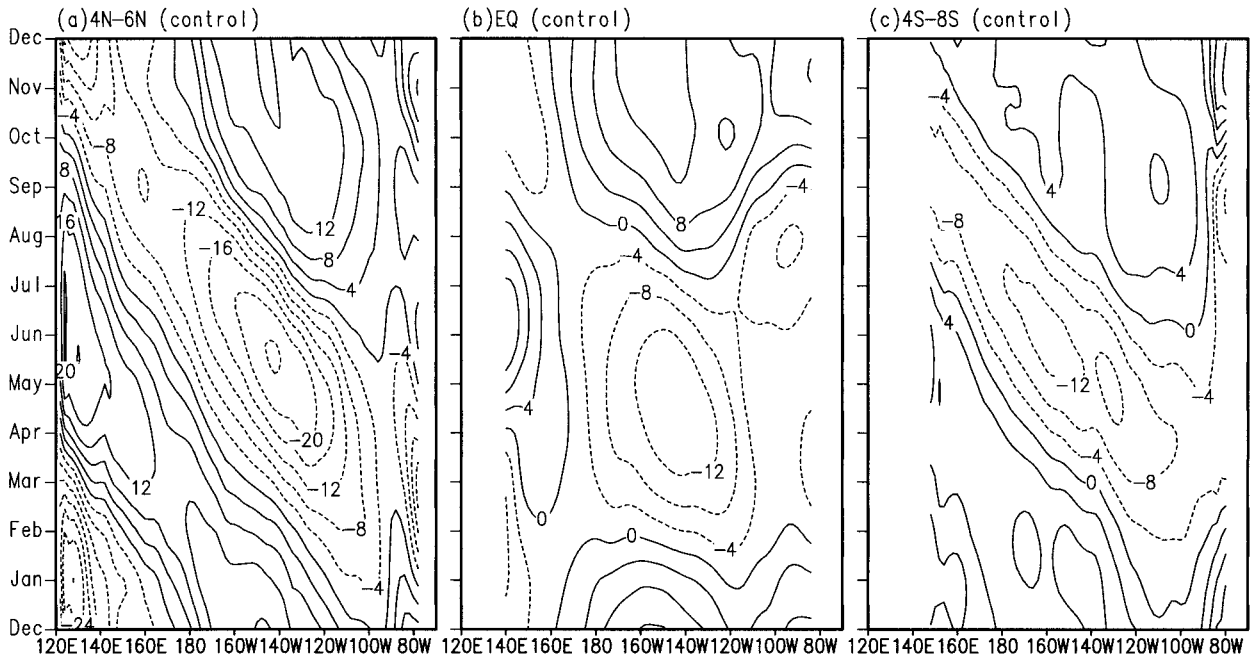

FIG. 10. Simulated time–longitude diagrams showing the annual thermocline departure along (a) 4°–6°N, (b) the equator, and (c) 4°–8°S, in the control experiment.

Sea (Fig. 12b). However, *the monsoon has little local effect in the latitude bands between 4°S and 10°S where westward propagation is prominent.* This results from the moderate amplitude of the annual variation of wind stress in situ (Fig. 3d). Remotely, the WPM has remarkable influence on the thermocline variation in the equatorial central and eastern Pacific (Fig. 12b). Additional experiments identify that the remote impacts are primarily attributed to the monsoon variability in the equatorial western Pacific, which affects the equatorial central and eastern Pacific through equatorial Kelvin waves. The suppression of the equatorial western Pacific wind annual cycle decreases the thermocline variability in the equatorial central Pacific while it increases thermocline variability in the equatorial eastern Pacific. Whether the equatorial western Pacific winds cause an increase or a decrease of the annual thermocline variability in the remote regions depends on the phase relation between the Kelvin waves forced by the equatorial western Pacific winds and the dominant local variations.

If the wind forcing in the ECP is suppressed (''noECP'' experiment), the annual variation of thermocline along 4°N and 4°S in the western Pacific significantly weakens (Fig. 12c), indicating that the westward propagation along the two latitudinal bands is strongly linked to the remote variations in the ECP. The latter also impact the thermocline variation in the equatorial eastern Pacific through Kelvin wave propagation along the equator.

6. Causes of the annual variation of the thermocline in the equatorial Pacific

a. The equatorial waveguide

In the ECP from 170°W to 120°W, the annual range is the largest in the equatorial waveguide with a maximum exceeding 24 m around 150°W (Fig. 3b). The unimodal variation in the ECP with the maximum in December and the minimum around May–June (Fig. 5b) is not controlled by the local wind forcing as revealed by the phase relationship between the local Ekman pumping and thermocline variation (Fig. 8). On the other hand, we see that the WPM is extremely influential on the thermocline variation in this region. Without the annual variation in WPM, the annual range in the core region of the ECP would decrease by more than 16 m (Fig. 12b) and would become a minimum in the equatorial waveguide. In addition, the December maximum would disappear (Fig. 13b) and the phases and associated propagation would also be totally different from those in the control run (Fig. 10b). With only the WPM forcing (the ''onlyWPM'' experiment), the thermocline variation in the ECP (Fig. 14b) bears a gross similarity to that in the control run. These results suggest that the WPM plays a key role in the annual variation of the thermocline in the ECP.

While the annual variation of the thermocline in the ECP is largely due to remote forcing from the WPM, the eastern Pacific ITCZ may play an important role in phasing the occurrence of the maximum and minimum

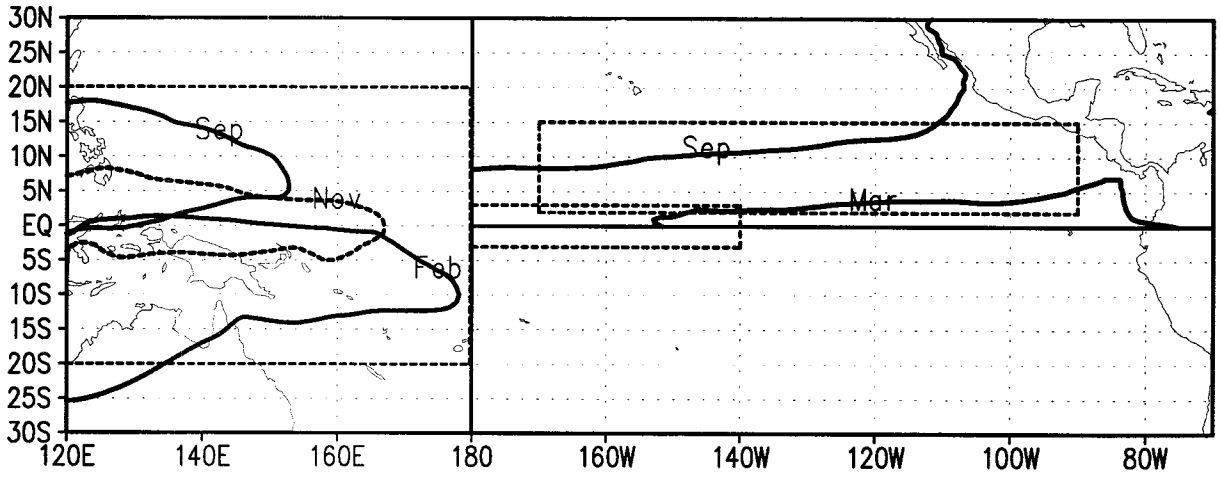

FIG. 11. Schematic diagram showing the zero contours of zonal wind stress in Feb, Sep, and Nov (west of date line) and the zero contours of the meridional wind stress in Mar and Sep (east of date line and north of the equator). The boxes enclosed by thick-dashed lines indicate the regions where annual wind stress departures are suppressed in the sensitivity experiments.

depths. From the observed evolution (Fig. 7), the establishments of both the December maximum and the May–June minimum in the ECP are closely associated with the development and subsequent westward and equatorward propagation of the annual departure induced by the annual March of the ITCZ. It is plausible that the wind forcing in the eastern Pacific ITCZ contributes to the timing of occurrence of the annual thermocline extremes. The experiment ''noITCZ'' does not show significant impact of the ITCZ on the ECP thermocline variation. This may be a result of the model deficiency. In the control run, the phases of the thermocline maxima and minima are about 1 month earlier than the observed (Figs. 6b and 10b). This discrepancy may be due to the model's underestimation of the beta dispersion and the influence of the ITCZ on the ECP thermocline variation.

In the equatorial western Pacific, the annual range is less than 16 m except in the far western Pacific (Fig. 3b). The annual variation around 170°E exhibits a minimum amplitude in the equatorial waveguide and a bimodal seasonal distribution (Fig. 4). The dominant bimodal variation with maxima occurring around November–May and minima around January–August is partially a rapid response to the equatorial western Pacific monsoon, which shows the largest westerly departure in November and a minor peak in April–May. In addition, the May maximum and August minimum are also closely related to the westward propagation of annual Rossby waves to the north and south of this region (Figs. 5 and 7). In the far equatorial western Pacific (west of 150°E), the annual cycle also displays a significant semiannual component with an annual maximum in April–May and an annual minimum in January–September. These extreme phases are not well related to local wind forcing as revealed by the phase difference between the local Ekman pumping and thermocline displacement (Fig. 8). Instead, they are determined by westward propagating Rossby waves north of the equator, which are remotely forced in the ITCZ and the ECP as shown by the phase propagation diagram (Fig. 5) and the results from ''noITCZ'' and ''noECP'' experiments (Figs. 12a,c).

In the equatorial eastern Pacific, the amplitude is again smaller than 16 m (Fig. 3b) and the annual thermocline variation contains a significant semiannual component (Fig. 4). The maximum depth occurs in January and the minimum in August–September (Fig. 5 and Fig. 6b). The January maximum appears to be associated with the eastward propagation of the maximum

TABLE 1. Numerical experiments.

Experiment	Region of interest	Change in the forcing stress
Control	All	No
noITCZ	Eastern Pacific ITCZ 2°–15°N, 170°–90°W	Annual variation is suppressed
noWPM	Western Pacific monsoon 20°S–20°N, west of date line	Annual variation is suppressed
noECP	Equatorial central Pacific 3°S–3°N, 180°–140°W	Annual variation is suppressed

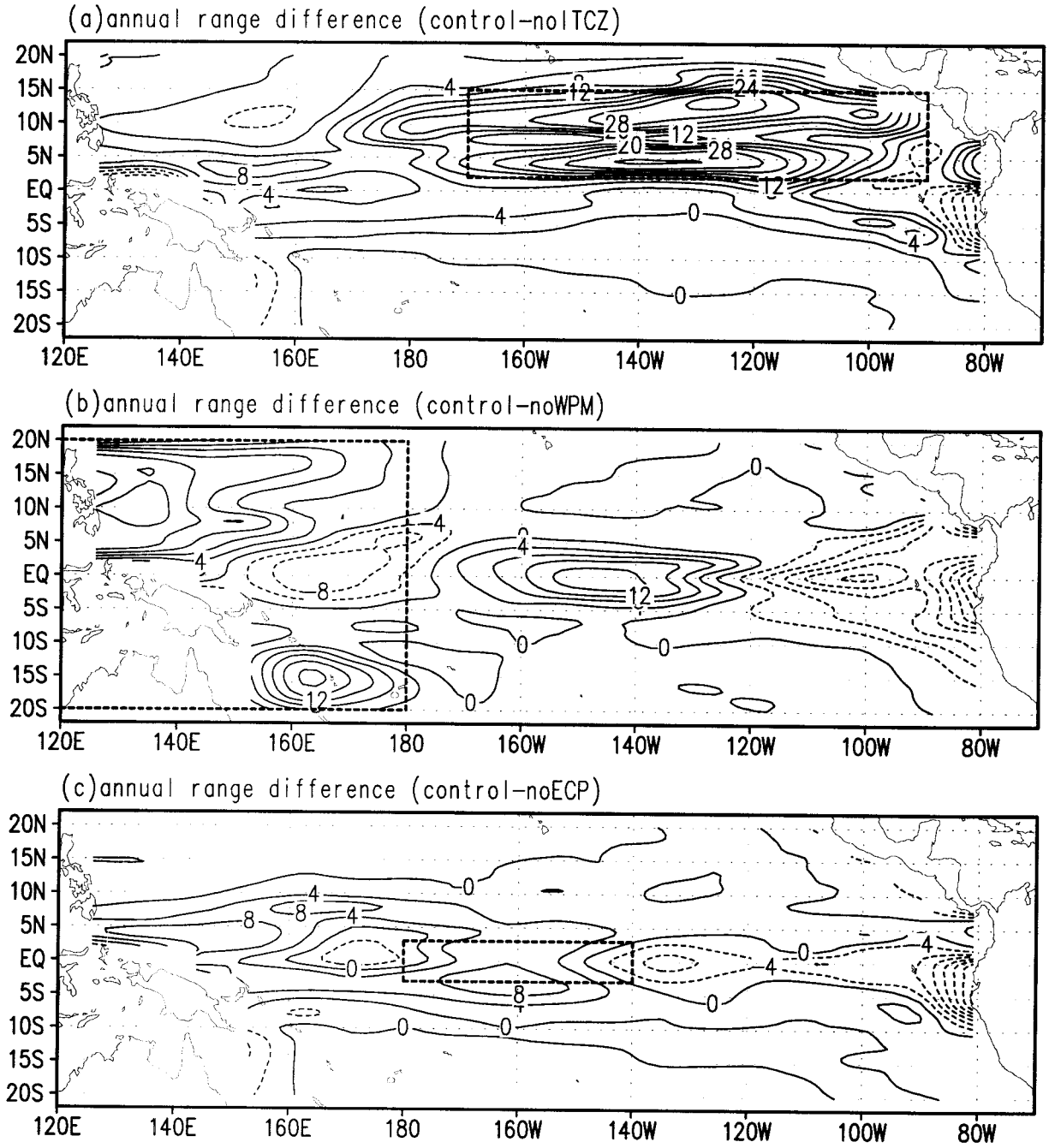

FIG. 12. The differences in the annual range between the control experiment and the (a) ''noITCZ'' experiment, (b) ''noWPM'' experiment, and (c) ''noECP'' experiment, respectively. The thick-dashed lines denote regions where annual wind stress departures are suppressed in the corresponding sensitivity experiments.

DTC from 140°W with a speed close to the lowest baroclinic Kelvin wave. Figure 12 shows that the thermocline in the equatorial eastern Pacific is very sensitive to the remote wind forcing from the ITCZ, WPM, and ECP. Thus, the thermocline variation in the far equatorial eastern Pacific is likely due to the combined effects of the remote forcing. Apparently, the remote forcing–induced variations are out of phase in general, resulting in a cancellation among various remote forcing effects, so that the resultant amplitude is small. Meyers (1979b) hypothesized that the semiannual variation of the 14°C isotherm in the eastern Pacific is due to remote forcing from the ECP wind, which has strong semiannual component. This hypothesis was tested and con-

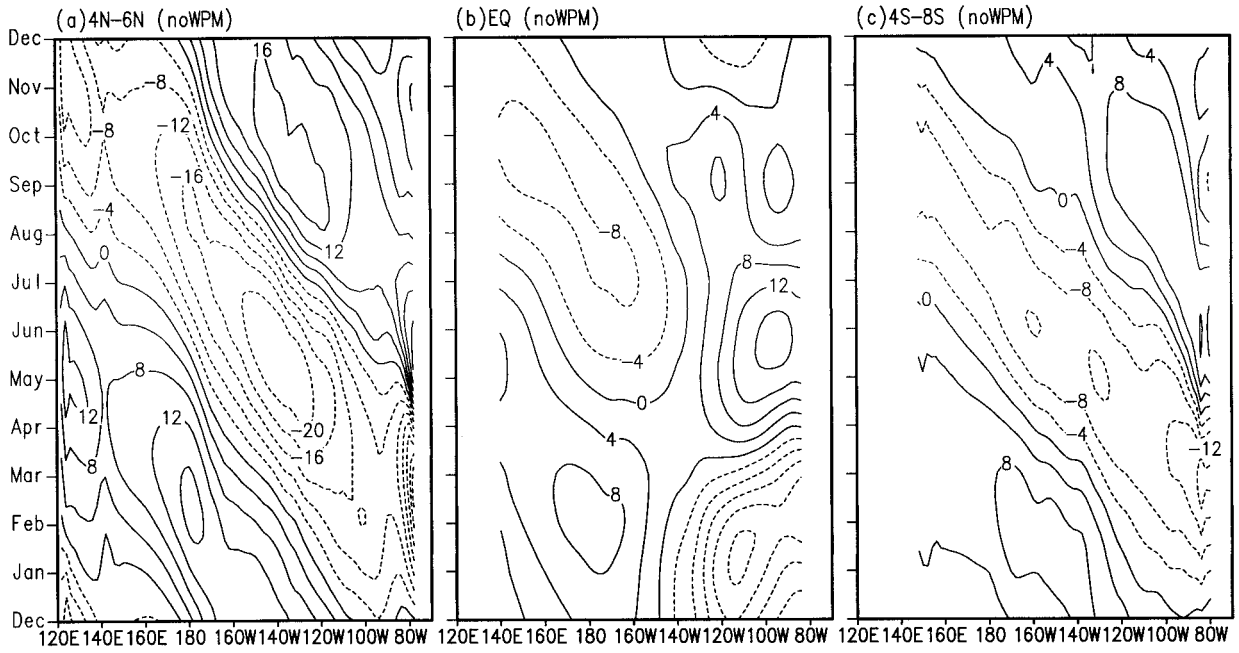

FIG. 13. The same as in Fig. 10 except for the experiment ''noWPM'' in which the annual wind stress departures are suppressed in the western Pacific monsoon region (20°S–20°N, west of date line).

firmed by Kindle (1979) using a nonlinear model and an analytical model and supported by the results of Busalacchi and O'Brien (1980) obtained using a simple linear model. The experiment ''ECP'' indicates that the ECP wind forcing is an important, but not the only, factor. Due to the inability of the model to reproduce the semiannual thermocline variation in the far eastern equatorial Pacific, we are not able to confirm this point unambiguously.

b. The off-equatorial westward propagation along 3°–7°N and 3°–9°S

Although a large portion of the off-equatorial westward phase propagation in DTC occurs primarily in the WPM region (Figs. 5 and 6a,c), the local monsoon forcing plays a minor role. This can be seen from Figs. 13a,c and 14a,c, which presents the phase propagation along 5°N and 6°S simulated in the ''noWPM'' and ''onlyWPM'' experiments, respectively. Comparison of these results with those of the control experiments (Figs. 10a,c), one may conclude that the WPM plays a minor role except in the far western North Pacific (west of 140°E) where the westward increases of annual amplitude (Fig. 10c) must be due to the local wind forcing. The prominent westward propagation from the central to western Pacific must be produced by Rossby waves remotely forced in the eastern-central Pacific. The averaged speed of 0.5–1.0 m s^{-1} can be reasonably thought of as the speeds of the equatorial Rossby waves with the lowest or second lowest meridional modes.

The propagation of the annual maximum and minimum starts from the ECP in December and June, respectively. The results of the experiments ''noECP'' and ''noITCZ'' shown in Figs. 12a,c demonstrate that suppression of the wind forcing in the ECP and the eastern Pacific ITCZ results in a significant weakening of the annual thermocline variation within the two off-equatorial Rossby waveguides. The contributions from the two remote forcing regions appear to be comparable. More important, the phases of the remotely forced Rossby waves are also nearly in phase (figure not shown).

7. Summary

On the annual timescale, the largest thermocline variability is found in each side of the mean position of the eastern Pacific ITCZ and in the off-equatorial regions of the western Pacific (Fig. 3b). These regions also feature the strongest annual variations in surface wind stress curl (Fig. 3d), suggesting that the annual march of the ITCZ and western Pacific monsoons outlined in Fig. 11 are the primary driving force for the annual thermocline variations of the tropical Pacific.

In the North Pacific poleward of 8°N and in the South Pacific poleward of 10°S, the downwelling (upwelling) Ekman pumping leads the thermocline deepening (rising) by about 1–4 months (Fig. 8), suggesting the controlling role of the local wind stress in the annual variation of the thermocline. The phase of the thermocline displacement is nearly stationary across the *interior* ba-

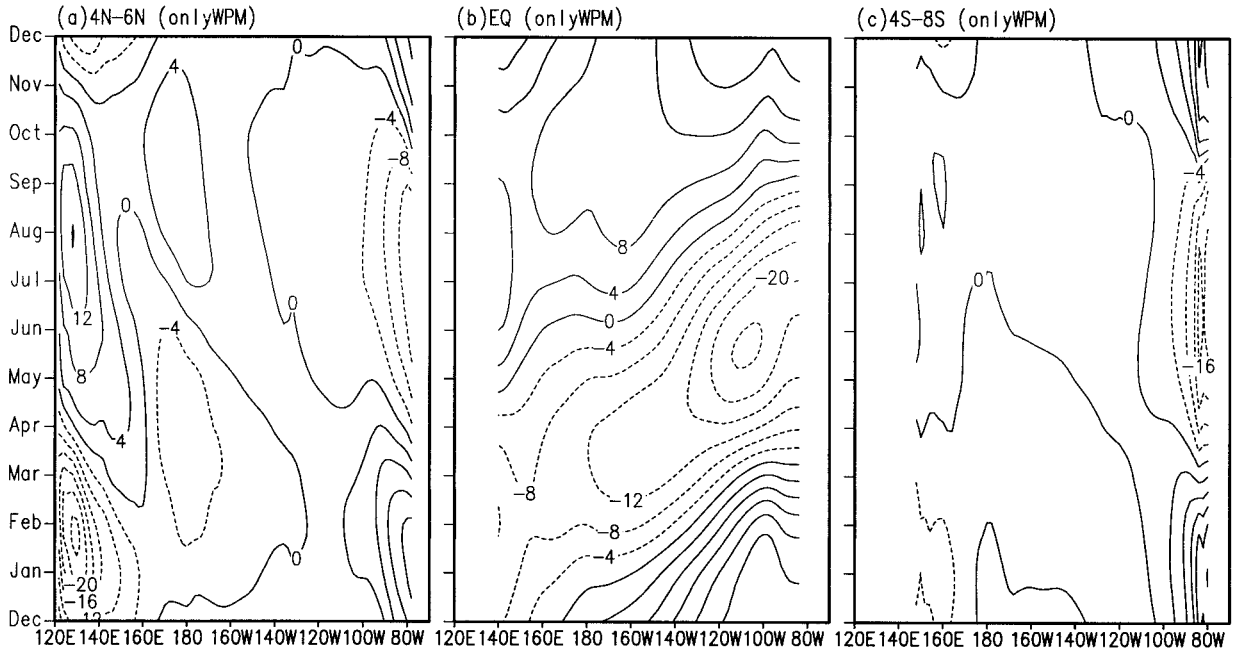

FIG. 14. The same as in Fig. 10 except for the experiment ''only WPM'' in which the annual wind stress departures are suppressed except in the western Pacific monsoon region (20°S–20°N, west of date line).

sin with the maximum (minimum) depth occurring during May–June (December) in the North Pacific and in October–November (April–May) in the South Pacific. Note that there are signals of westward propagation in the phase diagrams of the annual maximum and minimum depths in the North Pacific (Fig. 5), but they are confined to the ocean eastern boundary. To the lowest order approximation, the annual variations of thermocline between the two hemispheric off-equatorial trade wind regions form approximately an annual seesaw oscillation in response to the annual variations of the subtropical anticyclonic wind stress forcing.

In the region roughly between 8°N and 10°S, the annual adjustment of the thermocline is controlled by both the Ekman pumping and equatorial wave propagation.

The Ekman regime, in which local wind-induced Ekman pumping dominates, is found in the equatorward side of ITCZ in the central North Pacific (3°–8°N, 170°–120°W) where the thermocline exhibits the largest amplitude (centered at 4°N and 140°W; Fig. 3b) due to the pronounced annual variation of the wind stress curl south of the ITCZ (Fig. 3d). This assertion is supported by the phase lead of the local Ekman pumping to the thermocline displacement (Fig. 8) and by the numerical experiment without ITCZ forcing (Fig. 12a). It is important to note that, immediately to the south of this Ekman regime, in the ECP (2°N–5°S, 170°–120°W), the annual thermocline variability is also large (Fig. 3b). What is more important, the annual cycle displays a distinctive unimodal seasonal variation (deepest in December and shallowest in May–June), which is nearly in phase with the Ekman regime north of it (Fig. 5). Figure 7 shows that the annual march of ITCZ induces positive (negative) DTC departure in September (March) around 4°N, 110°W. The positive (negative) departures then propagate westward and equatorward due to Rossby wave dispersion. This contributes to the formation of the annual maximum (minimum) DTC in the ECP and suggests the remote impacts of the ITCZ on the ECP thermocline variation, in particular, in phasing the occurrence of the December maximum and May–June minimum depths. The pronounced annual variation in the ECP is also attributed to the remote forcing from the western Pacific monsoon via eastward propagation of annual downwelling Kelvin waves from November to January (Fig. 5). This can be seen from the results of the numerical experiment shown in Fig. 12b, which indicate that without western Pacific monsoon forcing the annual thermocline variability in the ECP is substantially suppressed. Therefore, the distinct ECP annual cycle of the thermocline variation is primarily caused both by remote forcing from the eastern Pacific ITCZ and by the western Pacific monsoon.

The wave regime, in which equatorial waves play a dominant role in the annual adjustment of the thermocline, also embraces two off-equatorial bands along 5°N (3°–7°N) and 6°S (3°–9°S) along which prominent westward Rossby wave propagation with a longitudinally varying speed (0.5–1.0 m s^{-1}) dominates. The annual Rossby waves are primarily excited in the ECP, after the formation of the annual maximum and minimum (Fig. 7). The annual maximum depth propagates

from the ECP in December to the western boundary in April, while the annual minimum propagates from the ECP in May to the western boundary in September (Fig. 5). These annual Rossby waves appear to be reflected from the western ocean boundary and affect the thermocline variation in the far western equatorial Pacific (Fig. 5).

In the western and eastern equatorial Pacific, the annual variations of thermocline are small and display a considerable semiannual component–bimodal variation. The bimodal variation in the western equatorial Pacific is partially driven by the monsoon westerlies and partially influenced by the reflected annual Rossby waves remotely forced in the central Pacific. The bimodal variations in the equatorial far eastern Pacific result from remote forcings through the Kelvin wave propagation.

The long-term mean and the annual variation of the thermocline may impact the ENSO evolution. The thermocline ridge along 7°–10°N separates the NEC and NECC and inhibits meridional transfer of water in the western Pacific except in the Mindanao Current region. This blocking effect is the weakest during May when the local ridge is the weakest. In the ECP, the thermocline is the deepest in December and the shallowest in May–June with prominent amplitude (Fig. 3b). This region of large annual variability coincides with the region of the largest zonal gradient in the mean thermocline depth. It also coincides with the Niño-3.4 region where SST variations are considered to be the most appropriate indication for describing ENSO (Trenberth 1997). The standard deviation of the interannual variation of SST there reaches a maximum in December (about 1°C) and a minimum in May (about 0.5°C). This may be the region where the annual cycle and ENSO interact considerably, but the precise manner of the interaction needs further investigation.

Acknowledgments. The authors acknowledge support from NOAA–OGP under GOALS and PACS programs and the support for the establishment of the Klaus Wyrtki Center for Climate Research and Prediction at the University of Hawaii. RL was supported under NSF Grant OCE-90 24452 (TOGA COARE). This is the School of Ocean and Earth Science and Technology publication No. 4917 and IPRC publication No. 24.

REFERENCES

Boulanger, J.-P., and L.-L. Fu, 1996: Evidence of Kelvin and first-mode Rossby waves from TOPEX/Poseidon sea level data. *J. Geophy. Res.,* **101,** 16 361–16 371.

Bryan, K., 1969: A numerical method for the study of the World Ocean. *J. Comput. Phys.,* **4,** 347–376.

Busalacchi, A. J., and J. J. O'Brien, 1980: The seasonal variability in a model of the tropical Pacific. *J. Phys. Oceanogr.,* **10,** 1929–1951.

Chang, P., 1994: A study of the seasonal cycle of sea surface temperature in the tropical Pacific Ocean using reduced gravity models. *J. Geophys. Res.,* **99,** 7725–7741.

Chelton, D. B., and M. G. Schlax, 1996: Global observations of ocean Rossby waves. *Science,* **272,** 234–238.

Cox, M. D., 1984: A primitive, 3-dimensional model of the ocean. GFDL Ocean Group Tech. Rep. No. 1, Geophysical Fluid Dynamics Laboratory, 143 pp. [Available from Geophysical Fluid Dynamics Laboratory, Princeton University, Princeton, NJ 08542.]

Derber, J., and A. Rosati, 1989: A global oceanic data assimilation system. *J. Phys. Oceanogr.,* **19,** 1333–1347.

Goldenberg, S. B., and J. J. O'Brien, 1981: Time and space variability of tropical Pacific wind stress. *Mon. Wea. Rev.,* **109,** 1190–1207.

Harrison, D. E., 1989: On climatological monthly mean wind stress and stress curl fields over the World Ocean. *J. Climate,* **2,** 57–70.

Hellerman, S., and M. Rosenstein, 1983: Normal monthly wind stress over the World Ocean with error estimates. *J. Phys. Oceanogr.,* **13,** 1093–1104.

Ji, M., A. Leetmaa, and J. Derber, 1995: An ocean analysis system for climate studies. *Mon. Wea. Rev.,* **123,** 460–481.

Kessler, W. S., 1990: Observations of long Rossby waves in the northern tropical Pacific. *J. Geophys. Res.,* **95,** 5183–5217.

——, and J. P. McCreary, 1993: The annual wind-driven Rossby wave in the subthermocline equatorial Pacific. *J. Phys. Oceanogr.,* **23,** 1192–1207.

——, and M. J. McPhaden, 1995: Oceanic equatorial waves and the 1991–1993 El Niño. *J. Climate,* **8,** 1757–1774.

Kindle, J. C., 1979: Equatorial Pacific Ocean variability—Seasonal and El Niño time series. Ph.D. dissertation, The Florida State University, 134 pp. [Available from Department of Meteorology, The Florida State University, Tallahassee, FL 32306.]

Leetmaa, A., and M. Ji, 1989: Operational hindcasting of the tropical Pacific. *Dyn. Atmos. Oceans,* **13,** 465–490.

Lukas, R., 1981: The termination of the equatorial undercurrent in the eastern Pacific. Ph.D. dissertation, University of Hawaii at Manoa, 127 pp. [Available from Department of Oceanography, University of Hawaii at Manoa, 1000 Pope Road, Honolulu, HI 96822.]

——, and E. Firing, 1985: The annual Rossby wave in the central equatorial Pacific Ocean. *J. Phys. Oceanogr.,* **15,** 55–67.

——, ——, P. Hacker, P. L. Richardson, C. A. Collins, R. Fine, and R. Gammon, 1991: Observations of the Mindanao current during the Western Equatorial Pacific Ocean Circulation Study. *J. Geophys. Res.,* **94** (C4), 7089–7104.

Masumoto, Y., and T. Yamagata, 1993: Simulated seasonal circulation in the Indonesia Seas. *J. Geophys. Res.,* **98** (C7), 12 501–12 509.

Meyers, G., 1979a: On the annual Rossby wave in the tropical North Pacific Ocean. *J. Phys. Oceanogr.,* **9,** 663–674.

——, 1979b: Annual variation in the slope of the 14°C isotherm along the equator in the Pacific Ocean. *J. Phys. Oceanogr.,* **9,** 885–891.

——, 1982: Interannual variation in sea level near Truk Island—A bimodal seasonal cycle. *J. Phys. Oceanogr.,* **12,** 1161–1168.

Minobe, S., 1996: Detection of an annual westward propagating signal in the meridional wind component along 8°N in the Pacific. *J. Climate,* **9,** 1661–1668.

Mitchum, G. T., and R. Lukas, 1990: Westward propagation of annual sea level and wind signals in the western Pacific Ocean. *J. Climate,* **3,** 1102–1110.

Murakami, T., B. Wang, and S. W. Lyons, 1992: Summer monsoons over the Bay of Bengal and the eastern North Pacific. *J. Meteor. Soc. Japan,* **70,** 191–210.

Niiler, P. P., and E. B. Kraus, 1977: One-dimensional models of upper ocean. *Modeling and Prediction of the Upper Layers of the Ocean.* E. B. Kraus, Ed., Pergamon Press, 143–172.

Oberhuber, J. M., 1988: An atlas based on the ''COADS'' dataset: The budgets of heat, buoyancy and turbulent kinetic energy at the surface of the global ocean. Report No.15, Max-Plank-Institut für Meteorologie, 20 pp. [Available from Max-Planck-Institut für Meteorologie, Bundesstr. 55 D-20146 Hamburg, Germany.]

Philander, S. G. H., W. J. Hurlin, and A. D. Seigel, 1987: Simulation of the seasonal cycle of the tropical Pacific Ocean. *J. Phys. Oceanogr.*, **17,** 1986–2002.

Reynolds, R. W., and T. M. Smith, 1994: Improved global sea surface temperature analysis using optimum interpolation. *J. Climate,* **7,** 929–948.

Sadler, J. C., M. A. Lander, A. M. Hori, and L. K. Oda, 1987: Tropical marine climate atlas. Vol. 1, Pacific Ocean. Report UHMET 87-02, Department of Meteorology, University of Hawaii, Honolulu, Hawaii, 27 pp. [Available from Department of Oceanography, University of Hawaii at Manoa, 1000 Pope Road, Honolulu, HI 96822.]

Smith, T. M., and M. Chelliah, 1995: The annual cycle in the tropical Pacific Ocean based on assimilated ocean data from 1983–1992. *J. Climate,* **8,** 1600–1614.

Trenberth, K. E., 1997: The definition of El Niño. *Bull. Amer. Meteor. Soc.*, **78,** 2771–2777.

Wang, B., 1994: Climatic regimes of tropical convection and rainfall. *J. Climate,* **7,** 1109–1118.

——, 1995: Interdecadal changes in El Niño onset in the last four decades. *J. Climate,* **8,** 267–285.

——, T. Li, and P. Chang, 1995: An intermediate model of the tropical Pacific Ocean. *J. Phys. Oceanogr.*, **25,** 1599–1616.

Wyrtki, K., 1961: Physical Oceanography of the southeast Asian waters. Naga Rep.2, 195 pp. [Available from Scripps Institution of Oceanography, La Jolla, CA 92093.]

——, 1974: Sea level and the seasonal fluctuations of the equatorial currents in the western Pacific Ocean. *J. Phys. Oceanogr.*, **4,** 91–103.

——, 1975: Fluctuations of the dynamic topography in the Pacific Ocean. *J. Phys. Oceanogr.*, **5,** 450–459.

Yang, Y.-J., T.-Y. Tang, and R. H. Weisberg, 1997: Basin-wide zonal wind stress and ocean thermal variations in the equatorial Pacific Ocean. *J. Geophys. Res.*, **102** (C1), 911–927.

Yu, X., and M. J. McPhaden, 1999: Seasonally variability in the equatorial Pacific. *J. Phys. Oceanogr.*, **29,** 925–947.

Zebiak, S. E., and M. A. Cane, 1987: A model El Niño–Southern Oscillation. *Mon. Wea. Rev.*, **115,** 2262–2278.